Robust Tube-MPC based Steering and Braking Control for Path Tracking at High-Speed Driving

Jonghyup Lee, Yoonjin Hwang, and Seibum B. Choi

***Abstract*—This paper proposes a steering and braking control strategy for stable path following at high speed in a robust model predictive control (MPC) framework. In severe driving situations, model uncertainties can cause control errors and lead to control failures. This paper introduces a method to minimize uncertainty and a controller that is robust against uncertainty. To minimize uncertainty, the proposed multi-point linearization reduces linearization error. Moreover, the used model minimizes the prediction errors due to the delays and lags of the actuators. The proposed controller, based on tube MPC, ensures the satisfaction of road friction limits for uncertain systems. Conditions to satisfy the feasibility of the MPC are proposed and proven. The proposed controller generates steering and braking inputs that ensure that none of the tires exceeds its friction limit. Simulation and experimental results in various test scenarios show the effectiveness of the proposed approach.**

***Index Terms*—Robust Model Predictive Control, Path Tracking Control, Model Linearization, Feasibility, Road Friction Limit**

I. Introduction

As the demand for vehicle safety and convenience increases, advanced driver assistance systems(ADAS) using cameras and radars are continuously developed. Certain ADAS functions have thus been recently evaluated as essential vehicle safety indicators. Path tracking control, which allows vehicles to follow a path generated by a path planner for a specific purpose, is essential for lateral ADAS [1]–[4]. Primary tracking controllers keep vehicles in lanes on highways or perform obstacle avoidance at low speeds. These ADAS devices thus aim at accurate tracking in stable and smooth driving conditions, during which vehicle speed is low or the steering angle is small.

However, with the development of technology, controller roles are expanding not only to smooth driving situations but also to dangerous situations. In particular, for path tracking at high speed, the dynamic safety of the vehicle must be considered because unstable behavior may occur due to tire friction limit. In addition, situations in which stable control cannot be achieved simply via steering control must be dealt with through appropriate braking control prior to steering.

In the literature, various algorithms for tracking control have been studied. Pure-pursuit [5], sliding mode control [6], linear quadratic Gaussian control [7], and nonlinear adaptive control [8] have been proposed. These control methods generally show excellent tracking performance in smooth driving situations. However, it is challenging to guarantee performance in high-speed situations that require consideration of the friction limit of tires. Model predictive control (MPC) predicts future behavior using a dynamic model. It is one of the most suitable methods of path-tracking control because it considers constraints as it generates optimal control inputs [9]–[21]. To deal with the model nonlinearity, nonlinear MPC has been proposed for path tracking [11]–[13]. However, real-time implementation is limited because of the significant computation burden of nonlinear programming. This problem has been addressed in various works in the literature by using linear MPC based on linearized models [14]–[17]. This method increases the prediction error but is essential for real-time controller implementation.

Also, in some path tracking control studies, robust MPC (RMPC) was utilized to resist model uncertainty or external disturbances. In [22], the nonlinear RMPC-based tracking controller was designed to be robust against friction coefficient uncertainty and external disturbances. In [23], a linear RMPC-based path tracking controller robust to mass uncertainty and road bank was proposed. In addition to path tracking control, a RMPC-based lane change decision algorithm using deterministic and probabilistic prediction of other participants' states was proposed [24]. In addition, a control method considering violation of constraints was introduced in a study of path tracking control for autonomous racing [25] and four wheel steering and direct yaw-moment control [26] using tube based RMPC. Existing practical research based on RMPC can be highly valuable for performing constraint-satisfying in real-world applications. However, further discussion is needed on the overly conservative approach taken in setting constraints and ensuring feasibility in a practical sense.

Depending on the purpose of vehicle control using MPC, various works usually consider constraints such as yaw rate [17]–[20], [26], lateral position [20], acceleration [21], [25], side slip angle [18], and longitudinal tire force [27]. In particular, vehicle stability is governed by the friction limits of the tires, which can be considered indirectly in a linear manner through constraints such as yaw rate and side slip angle. In addition, in severe driving conditions where the load transfer of each wheel changes rapidly, the limits of the tire force of each wheel can be considered directly to ensure more accurate stability [27]. However, in models with combined longitudinal, lateral, and vertical motions, the tire force of each wheel has a large nonlinearity and should be utilized with appropriate measures.

Model uncertainties are caused by errors in the model

Jonghyup Lee is with the Hyundai Motor Company, Seoul 06182, South Korea (e-mail: jonghyup.lee@hyundai.com).

Yoonjin Hwang and Seibum Choi (Corresponding author) are with the Korea Advanced Institute of Science and Technology (KAIST), 291, Daehak-ro Yuseong-gu, Daejeon, 34141, South Korea (e-mail: yoonjinh@kaist.ac.kr;sbchoi@kaist.ac.kr).

linearization process, lags and delays of sub-controllers and actuators, and model parameter errors. In general, they degrade the prediction accuracy of MPC and cause tracking errors. In particular, in dangerous driving situations where the road friction limit must be considered, these may cause not only simple errors but also unexpected and unstable vehicle behavior, which may cause control failure. Therefore, both an effort to reduce the size of these uncertainties and the design of a robust controller are required.

In recent studies, robust MPC was applied to attenuate uncertainties and disturbances for path tracking. Mayne et al. first proposed the tube MPC as an effective method of robust MPC, ensuring that state constraints are not violated for bounded disturbances of linear time-invariant (LTI) systems [28]. Bumroongsri et al. extended this method for linear time-varying (LTV) systems [29]–[31]. The input obtained from the tube MPC consists of the nominal MPC input and feedback input for errors between actual and nominal states. The additional feedback input effectively reduces the effect of uncertainty, and satisfaction of constraints is guaranteed through tightened constraints that consider the effect of uncertainty.

Overall, the primary purpose of this study is the integrated control of steering and braking for stable path tracking at high speed. For this, methods to minimize uncertainties and a robust MPC are proposed. The newly proposed multi-point linearization model minimizes uncertainty in the linearization process. We linearized the nonlinear model for the states predicted in the previous step. The proposed method effectively reduces the linearization error by minimizing the distance between the linearization point and the actual states. In addition, the existing effective method, the delay-lag augmented model, was used to minimize the uncertainties caused by delays and lags of actuators [32], [33]. This model avoids excessive uncertainties and performance degradation caused by ignoring delays and lags. For robustness against uncertainties remaining despite the above efforts, the tube MPC framework was used. In addition, new conditions for feasibility against additional model mismatch caused by multi-point linearization are presented and proved.

The main contributions of this article can be summarized as follows:

1) For stable path tracking in high-speed situations, a tube MPC-based integrated steering, and braking controller that satisfies the road friction limit is proposed.

2) A multi-point linearized vehicle model that consider the performance of the sub-controller is proposed to minimize model uncertainties.

3) Conditions to satisfy the feasibility of MPC are proposed even if the model change due to linearization.

4) Constraint tightenings considering a robust invariant set and feasibility conditions are calculated off-line practically using driving data.

Finally, the proposed controller shows stable path tracking performance despite the model's nonlinearity and actuator performance limitations. In particular, even without a separate speed planner, optimal braking is performed before steering to prevent tire forces from exceeding their limits during turning. Simulation and experimental results in various scenarios show the effectiveness of the proposed approach. The proposed controller automatically carries out braking control when safe control is impossible with steering alone. Note that the proposed controller does not address throttle control, as the focus is on effective safety control for emergencies.

The rest of this paper is organized as follows. Section II introduces a linearized vehicle model that considers actuator delay and lag. Section III briefly summarizes the structure and characteristics of tube MPC for LTV systems. The proposed controller is described in detail in section IV. In section V and section VI, the performance of the proposed controller is verified through simulation and experiment, respectively. Finally, section VII provides a conclusion.

A. Notation

I_m denotes an m-dimensional identity matrix, and $O_{m\times n}$ denotes m-by-n zero matrix. Set operations such as Minkowski set addition $X \oplus Y := \{x+y|x\in X, y\in Y\}$, and Pontryagin set difference $X \ominus Y := \{x|x\oplus Y \subseteq X\}$ will be used. A set of integers is defined by $\mathbb{N}_a^b := \{n\in\mathbb{N}|a\le n\le b\}$. $\mathrm{Conv}\{\cdot\}$ denotes the convex hull of the elements in $\{\cdot\}$.

II. Vehicle model

In this section, we present the mathematical models used for control design. The model designed from the non-linear vehicle and tire model is expressed as a linear model through linearization, and delays and lags of the inputs are compensated. The subsection II-A introduces the vehicle dynamics model, the subsection II-B introduces the model linearization, and the subsection II-C introduces an augmented model that considers the performance of the actuators:

A. Nonlinear Vehicle Model

We used the following equations to express the vehicle motions and the positional relationship with respect to the desired path shown in Figure 1 [10], [34], [35].

$$\begin{aligned}
\dot{v_x} =& \frac{1}{m}[\left(F_x^{fl}+F_x^{fr}\right)\cos\delta\ + F_x^{rl}+F_x^{rr} \\
&-\left(F_y^{fl}+F_y^{fr}\right)\sin\delta\ - c_d(v_x)^2] + v_x\beta\dot{\psi}, && (1)\\
\dot{\beta} =& \frac{1}{mv_x}[\left(F_x^{fl}+F_x^{fr}\right)\sin\delta\ + \left(F_y^{fl}+F_y^{fr}\right)\cos\delta \\
&+F_y^{rl}+F_y^{rr}] - \dot{\psi}, && (2)\\
I_z\ddot{\psi} =& l_f[\left(F_y^{fl}+F_y^{fr}\right)\cos\delta + \left(F_x^{fl}+F_x^{fr}\right)\sin\delta] \\
&- l_r\left(F_y^{rl}+F_y^{rr}\right) + b[(F_y^{fl}-F_y^{fr})\sin\delta \\
&+(F_x^{fr}-F_x^{fl})\cos\delta\ + (F_x^{rr}-F_x^{rl})], && (3)\\
\dot{s} =& v_x\left(\cos e_\psi - \beta\sin e_\psi\right), && (4)\\
\dot{e_y} =& v_x\left(\sin e_\psi - \beta\cos e_\psi\right), && (5)\\
\dot{e_\psi} =& \dot{\psi} - \kappa(s)\dot{s}, && (6)
\end{aligned}$$

where, v_x is the vehicle speed, β is the side slip angle, $\dot{\psi}$ is the yaw rate, s is the station(longitudinal position on the desired path), e_y and e_ψ are the lateral and yaw angle errors

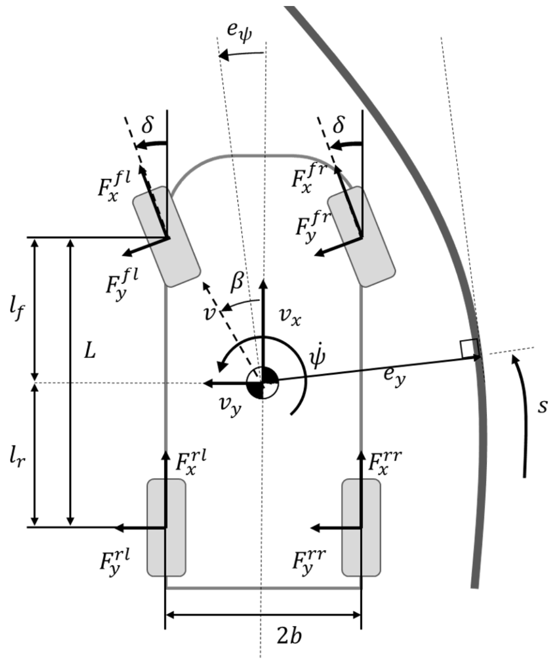

Figure 1. Nonlinear vehicle model

for the desired path. F_x and F_y denote each tire's longitudinal and lateral forces, and δ is the steering angle. The superscripts fl,fr,rl, and rr represent the front left, front right, rear left, and rear right wheels. The model parameters include vehicle mass (m), yaw moment of inertia (I_z), half of vehicle width (b), coefficient of air resistance (c_d), and distances from vehicle CG to front and rear axle (l_f,l_r). The road curvature κ is defined as a function of s.

The longitudinal tire forces are calculated from (1) as follows:

$$\begin{aligned}
F_x^{fl} = F_x^{fr} =& \frac{\lambda}{2\left[1-\lambda\left(1-\cos\delta\ \right)\right]} \\
&\left[ma_x + \left(F_y^{fl}+F_y^{fr}\right)\sin\delta\ + c_d(v_x)^2\right], \\
F_x^{rl} = F_x^{rr} =& \frac{(1-\lambda)}{2\left[1-\lambda\left(1-\cos\delta\ \right)\right]} \\
&\left[ma_x + \left(F_y^{fl}+F_y^{fr}\right)\sin\delta\ + c_d(v_x)^2\right],
\end{aligned} \tag{7}$$

where λ is the braking ratio, and a_x is the longitudinal acceleration.

The lateral tire forces are calculated by the brush tire model [36], [37].

$$\begin{aligned}
&F_y^j = C_\alpha(\tan\alpha^j) \\
&= \begin{cases} 3\mu F_z^j\theta_y\tan\alpha^j\{1-\left|\theta_y\tan\alpha^j\right| & +1/3(\theta_y\tan\alpha^j)^2\} \\ & ,\text{if}\tan\left|\alpha^j\right| < 1/\theta_y, \\ \\ \mu F_z^j \operatorname{sgn}\left(\alpha^j\right) & ,\text{if}\tan\left|\alpha^j\right| > 1/\theta_y, \end{cases}
\end{aligned} \tag{8}$$

where θ_y, μ and F_z are the model parameter, tire friction limit and each tire's normal force. The tire slip angle of each tire α^j can be expressed as:

$$\alpha^j = \tan^{-1}\frac{v_{ty}^j}{v_{tx}^j}, \tag{9}$$

where the wheel speeds in each direction on the each wheel coordinate are as follows:

$$\begin{aligned}
v_{tx}^j &= \begin{cases} -v_{w,x}^j\sin\delta + v_{w,y}^j\cos\delta & ,j=fl,fr, \\ -v_{w,x}^j & ,j=rl,rr, \end{cases} \\
v_{ty}^j &= \begin{cases} v_{w,x}^j\cos\delta + v_{w,y}^j\sin\delta & ,j=fl,fr, \\ v_{w,y}^j & ,j=rl,rr, \end{cases}
\end{aligned} \tag{10}$$

longitudinal velocity $v_{w,x}^j$ and lateral velocity $v_{w,y}^j$ of each wheel on the vehicle coordinate are calculated from v_x, β, and $\dot{\psi}$.

Remark 1. *The use of a tire model based on pure lateral slip may introduce modeling errors in combined longitudinal and lateral motion scenarios. However, in this study, the effect of longitudinal slip on the lateral tire force was ignored during the modeling phase to reduce the complexity of the model by constructing the model for the control input, longitudinal acceleration. The resulting modeling errors, along with other uncertainties, are robustly handled by the robust MPC discussed in Section IV.*

The normal forces, taking the load transfer into account, are given as:

$$\begin{aligned}
F_z^{fl} &= \frac{l_r}{2L}mg - \frac{h_{cg}}{2L}ma_x + \sigma_f ma_y, \\
F_z^{fr} &= \frac{l_r}{2L}mg - \frac{h_{cg}}{2L}ma_x - \sigma_f ma_y, \\
F_z^{rl} &= \frac{l_f}{2L}mg + \frac{h_{cg}}{2L}ma_x + \sigma_r ma_y, \\
F_z^{rr} &= \frac{l_f}{2L}mg + \frac{h_{cg}}{2L}ma_x - \sigma_r ma_y,
\end{aligned} \tag{11}$$

where L, g, a_y, and h_{cg} are the distance from the front axle to the rear axle, gravitational acceleration, lateral acceleration, and height of vehicle CG. Considering the roll stiffness of the front $c_{\phi f}$ and rear $c_{\phi r}$ axles [34], the lateral load transfer coefficients σ_f, σ_r are:

$$\begin{aligned}
\sigma_f &= \frac{1}{b}\left(\frac{c_{\phi f}h_{rc}}{c_{\phi f}+c_{\phi r}-mgh_{rc}} + \frac{l_r}{L}(h_{cg}-h_{rc})\right), \\
\sigma_r &= \frac{1}{b}\left(\frac{c_{\phi r}h_{rc}}{c_{\phi f}+c_{\phi r}-mgh_{rc}} + \frac{l_f}{L}(h_{cg}-h_{rc})\right),
\end{aligned} \tag{12}$$

where h_{rc} is the distance from CG to roll center.

By integrating and discretizing equations (1)-(12), the integrated nonlinear vehicle model can be expressed.

$$\begin{aligned}
x_o(k+1) &= f_k\left(x_{o,n}(k), u_o(k)\right) + \omega_{o,n}(k), \\
y(k) &= g_k\left(x_{o,n}(k), u_o(k)\right),
\end{aligned} \tag{13}$$

where, $x_o = [v_x, \beta, \dot{\psi}, s, e_y, e_\psi]^T \in \mathbb{R}^6$, $u_o = [\delta, a_x]^T \in \mathbb{R}^2$, $y = \left[\left(F_n^{fl}\right)^2, \left(F_n^{fr}\right)^2, \left(F_n^{rl}\right)^2, \left(F_n^{rr}\right)^2\right]^T \in \mathbb{R}^4$, and $\omega_{o,n} \in \mathbb{R}^6$ is the uncertainty caused by model parameter errors. The normalized tire forces F_n^j are defined as:

$$F_n^j = \sqrt{\frac{(F_x^j)^2+(F_y^j)^2}{(F_z^j)^2}}, \forall j \in fl, fr, rl, rr. \tag{14}$$

The system output vector y composed of the force of each wheel is used for the constraint of the controller later.

B. Linearized Vehicle Model

The nonlinear model (13) is linearized for the linearization points $(x_{lin}(k), u_{lin}(k))$ using Taylor expansion.

$$\begin{aligned} x_o(k+1) &= A_o(k)x_o(k) + B_o(k)u_o(k) + E_o(k) + \omega_o(k), \\ y(k) &= C_o(k)x_o(k) + D_o(k)u_o(k) + F_o(k) + \omega_{y,o}(k), \end{aligned} \tag{15}$$

where,

$$\begin{aligned} &A_o(k) = \nabla_x f_k(x,u)|^{x_{lin}(k)}_{u_{lin}(k)},\, B_o(k) = \nabla_u f_k(x,u)|^{x_{lin}(k)}_{u_{lin}(k)}, \\ &E_o(k) = f_k(x_{lin}(k), u_{lin}(k)) - A_o(k)x_{lin}(k) - B_o(k)u_{lin}(k), \\ &C_o(k) = \nabla_x g_k(x,u)|^{x_{lin}(k)}_{u_{lin}(k)},\, D_o(k) = \nabla_u g_k(x,u)|^{x_{lin}(k)}_{u_{lin}(k)}, \\ &F_o(k) = g_k(x_{lin}(k), u_{lin}(k)) - C_o(k)x_{lin}(k) - D_o(k)u_{lin}(k), \end{aligned} \tag{16}$$

and $\omega_o \in \mathbb{R}^6$ and $\omega_{y,o} \in \mathbb{R}^2$ include $\omega_{o,n}$ and linearization error. The selection of the linearization point has a great influence on the linearization error. The choice of $(x_{lin}(k), u_{lin}(k))$ to reduce the error is discussed in IV-B.

C. Compensation for Input Delays and Lags

The commanded input is delayed due to communication delay and mechanical clearance and is applied to the vehicle. Also, phase lag occurs due to the dynamics of the actuators and the sub-controllers. Input delays and lags are approximated by a first-order linear system as follows:

$$\begin{aligned} \tau_{l,\delta}\dot{\delta}(t) &= -\delta(t) + \delta_{in}(t - \tau_{d,\delta}), \\ \tau_{l,a_x}\dot{a_x}(t) &= -a_x(t) + a_{x,in}(t - \tau_{d,a_x}), \end{aligned} \tag{17}$$

where, $\tau_{l,*}$ are the time constants, $\tau_{d,*}$ are the input delays, δ_{in} and $a_{x,in}$ are the input command.

In order to identify the delays and lags of the control inputs, we compared the commands and measurements of the inputs as shown in Figure 2. In our experimental platform, the input delays are both 0.2s, and the time constants were identified as 0.1s and 0.01s for δ and a_x, respectively. The delayed and lagged commands by (17) shown in Figure 2 match the actual inputs well.

By combining (15) and (17), a model considering input lags is expressed as follows:

$$\begin{aligned} x_l(k+1) =& A_l(k)x_l(k) + B_l(k)\begin{bmatrix} \delta_{in}(k - k_{d,\delta}) \\ a_{x,in}(k - k_{d,a_x}) \end{bmatrix} \\ &+ E_l(k) + \omega_l(k), \end{aligned} \tag{18}$$

where,

$$x_l(k) = [x_o(k)^T, u_o(k)^T]^T,\ A_l(k) = \begin{bmatrix} A_o(k) & B_o(k) \\ O_{2\times6} & L_1 \end{bmatrix},$$

$$B_l(k) = \begin{bmatrix} O_{6\times2} \\ L_2 \end{bmatrix},\ E_l(k) = \begin{bmatrix} E_o \\ O_{2\times1} \end{bmatrix},\ k_{d,*} = \tau_{d,*}/T_s,$$

$$L_1 = \begin{bmatrix} e^{-\frac{T_s}{\tau_{l,\delta}}} & 0 \\ 0 & e^{-\frac{T_s}{\tau_{l,a_x}}} \end{bmatrix},\ L_2 = \begin{bmatrix} 1 - e^{-\frac{T_s}{\tau_{l,\delta}}} & 0 \\ 0 & 1 - e^{-\frac{T_s}{\tau_{l,a_x}}} \end{bmatrix},$$

$$\omega_l(k) = \begin{bmatrix} \omega_o(k) \\ O_{2\times1} \end{bmatrix},$$

and T_s is time interval of discrete system (13).

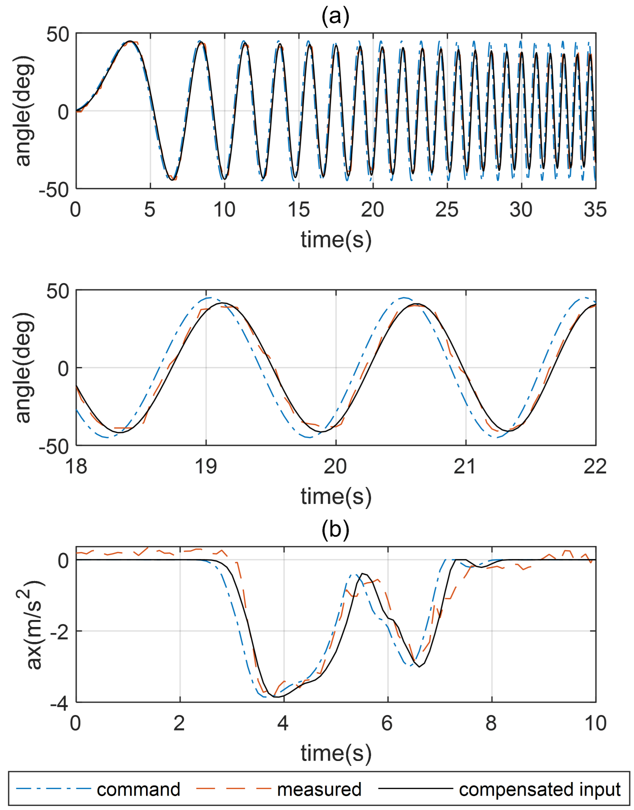

Figure 2. Identification of delays and lags of inputs

Input delays are handled through a delay-augmented model. The system is expressed in terms of a state vector incorporating delayed commands. Detailed descriptions of this approach are in [32], [33]. Since the time interval of the proposed controller is set to 0.1s (i.e. $T_s = 0.1$s), delays of 2 steps occur for both inputs (i.e. $k_{d,\delta} = k_{d,a_x} = 2$). The delay augmented model for a 2 steps delay is expressed as:

$$x(k+1) = A(k)x(k) + B(k)u(k) + E(k) + \omega(k), \tag{19}$$

where,

$$x(k) = [x_l(k)^T, u(k-2)^T, u(k-1)^T]^T \in \mathbb{R}^{12},$$

$$u(k) = \begin{bmatrix} \delta_{in}(k) \\ a_{x,in}(k) \end{bmatrix} \in \mathbb{R}^2,\ \omega(k) = \begin{bmatrix} \omega_l(k) \\ O_{4\times1} \end{bmatrix} \in \mathbb{W} \subseteq \mathbb{R}^{12},$$

$$A(k) = \begin{bmatrix} A_l(k) & B_l(k) & & \\ & & 1 & 0 \\ & & 0 & 1 \\ & & 0 & 0 \\ & & 0 & 0 \end{bmatrix} \in \mathbb{A},$$

$$B(k) = \begin{bmatrix} O_{8\times2} \\ 0 \quad 0 \\ 0 \quad 0 \\ 1 \quad 0 \\ 0 \quad 1 \end{bmatrix} \in \mathbb{B},\ \text{and}\ E(k) = \begin{bmatrix} E_l \\ O_{4\times1} \end{bmatrix} \in \mathbb{E}.$$

Therefore, the system model is expressed as a delay-free LTV system, and the system output vector is expressed as follows in the same way.

$$y(k) = C(k)x(k) + F(k) + \omega_y(k). \tag{20}$$

where, $y(k) \in \mathbb{Y} \subseteq \mathbb{R}^4, C(k) = \begin{bmatrix} C_o(k) & D_o(k) & O^{4\times4} \end{bmatrix} \in \mathbb{C} \subseteq \mathbb{R}^{4\times12}, F(k) = F_o(k) \in \mathbb{F}$, and $\omega_y(k) \in \mathbb{W}_y \subseteq \mathbb{R}^4$.

III. Background on tube MPC

In this section, we outline the framework used to develop tube-based robust MPC in section IV. Consider the nominal system of (19) to be defined as:

$$\bar{x}(k+1) = A(k)\bar{x}(k) + B(k)\bar{u}(k) + E(k). \tag{21}$$

Let $K(k) \in \mathbb{R}^{2\times12}$ be a feedback gain calculated in real time, such that $A^K(k) = A(k) + B(k)K(k)$ is stable, i.e. $A^K(k)$ is Hurwitz. If the system inputs (19) is defined as :

$$u(k) = \bar{u}(k) + K(k)e(k), \tag{22}$$

the error dynamics of $e(k) = x(k) - \bar{x}(k)$ is expressed as:

$$\begin{aligned} e(k+1) &= A(k)e(k) + B(k)K(k)e(k) + \omega(k) \\ &= A^K(k)e(k) + \omega(k). \end{aligned} \tag{23}$$

Therefore, the stable matrix $A^K(k)$ suppresses the error between the actual and nominal states caused by uncertainty. $e(k)$ is bounded to the robust positive invariant set Z defined for the LTV system as follows: [29]–[31]

Definition III.1. *The set Z is a robust positively invariant set of (23), if $A^K(k)Z + \mathbb{W} \subseteq Z$ for $\forall e(k) \in Z, \forall w(k) \in \mathbb{W}, \forall A(k) \in \mathbb{A}$, and $\forall B(k) \in \mathbb{B}$.*

The definition of robust positive invariant set was first defined for the LTI system [28] and was extended for the LTV system [30], [31]. The robust positive invariant set is calculated for all arbitrary matrices existing in sets $\mathbb{A}$ and $\mathbb{B}$, as follows:

$$\begin{aligned} &Z = \mathbb{W} \oplus \mathrm{Conv}\{A_p^K\mathbb{W}, \forall A_p \in \mathbb{A}, \forall B_p \in \mathbb{B}\} \\ &\oplus \mathrm{Conv}\{A_p^K A_q^K\mathbb{W}, \forall A_p, A_q \in \mathbb{A}, \forall B_p, B_q \in \mathbb{B}\} \oplus .... \end{aligned} \tag{24}$$

Proposition III.2. *Suppose the Z is a robust positively invariant set of the system (23), $\forall A(k) \in \mathbb{A}, \forall B(k) \in \mathbb{B}$. If $x(k) \in \bar{x} \oplus Z$ and $u(k) = \bar{u}(k) + K(k)e(k)$, then $x(k+1) \in \bar{x}(k+1) \oplus Z, \forall \omega(k) \in \mathbb{W}, \forall A(k) \in \mathbb{A}, \forall B(k) \in \mathbb{B}$.*

Proposition III.2 states the feedback policy keeps the states of the uncertain system close to the states of the nominal system. Therefore, if a feasible solution exists for the following tightened constraint of the nominal system (21), the control law (22) guarantees the satisfaction of the constraint for the uncertain system (19) [28], [30], [31].

$$\begin{aligned} &\bar{x}(k) \in \bar{X} \subseteq X \ominus Z, \\ &\bar{u}(k) \in \bar{U} \subseteq U \ominus KZ, \forall K \in \mathbb{K}. \end{aligned} \tag{25}$$

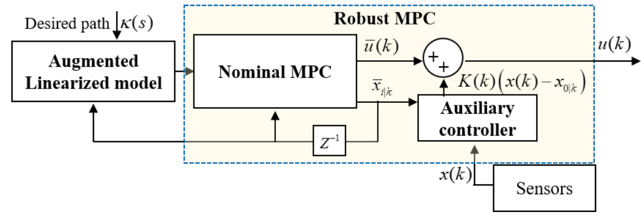

Figure 3. Control structure of the proposed controller

Also, for the constraint for the output function (20), if the nominal output satisfies the following tightened constraint, the constraint satisfaction of the original system is guaranteed.

$$\bar{y}(k) \in \mathbb{Y} \ominus \tilde{\mathbb{Y}}_Z, \tag{26}$$

where,

$$\tilde{\mathbb{Y}}_Z = \mathbb{W}_y \oplus \mathrm{Conv}\{C(k)Z, \forall C(k) \in \mathbb{C}\}. \tag{27}$$

IV. Controller design

This section introduces the design of RMPC for path tracking. In subsection IV-A, the cost function and constraint for path tracking are defined, and the optimization problem is also defined. In subsection IV-B , multi-point linearization is introduced to reduce linearization errors. In subsection IV-C, feasibility conditions are presented to solve model change due to multi-point linearization. Finally, subsection IV-D introduces a practical calculation of tightened constraints.

A. Control Structure

The purpose of the proposed controller is to accurately follow the desired path without exceeding the road friction limit of any tire and to be robust against uncertainty. In order to achieve these goals, tube-based RMPC introduced in section III is used. The overall control structure is shown in Figure 3. The controller consists of a nominal MPC that generates an optimal feedforward input and an auxiliary feedback controller to improve robustness.

For constrained optimization, cost function is defined as follows:

$$J = \sum_{i=0}^{N-1} q_{e_y}(\bar{e}_{y,i+1|k})^2 + q_{a_x}(\bar{a}_{x,i+1|k})^2 + \Delta\bar{u}_{i|k}^T \bar{R} \Delta\bar{u}_{i|k}, \tag{28a}$$

where, the subscript $i|k$ denotes the prediction value at (k+i)-th step predicted at the k-th step. q_{e_y} and q_{a_x} are each a positive gain that inhibits lateral error e_y and longitudinal acceleration a_x. This allows the control inputs to be calculated to minimize lateral error and suppresses braking in situations where braking is not necessary. And $\bar{R}$ is a positive diagonal matrix that suppresses the occurrence of jerk due to excessive input change $\Delta\bar{u}$ defined as follows:

$$\Delta\bar{u}_{i|k} = \begin{cases} \bar{u}_{i|k} - \bar{u}(k-1) & \text{if,} \quad i = 0 \\ \bar{u}_{i|k} - \bar{u}_{i-1|k} & \text{if,} \quad i \in \mathbb{N}_1^{N-1}. \end{cases}$$

Remark 2. *The primary objective of proposed controller is efficient trajectory tracking through lateral error minimization. Accurate path tracking under severe driving conditions necessitates appropriate side slip angles and headings during transient segments, as detailed in [38]. Excluding lateral errors, additional costs related to lateral motion states may even interfere with path tracking in some severe driving situations. The proposed controller uses an integrated vehicle model that considers yaw rate, lateral slip angle, heading angle error, and lateral error dynamics. Therefore, the optimization results for the proposed cost function are also used to plan for other lateral states to minimize the lateral error. The proposed cost function is effective for the purpose of this controller, but other forms may be more suitable for different purposes.*

Also, constraint is defined as follows:

$$\left(F^{j}_{n,i|k}\right)^2 \leq \mu^2, \forall i \in \mathbb{N}_0^{N-1}, \forall j \in fl, fr, rl, rr.. \quad (29a)$$

The constraint (29a) ensures that all tire forces do not exceed the friction limit during prediction. For the original system (19), the original constraint (29a) is expressed by (20) as:

$$y_{i|k} = (C_{i|k}x_{i|k} + F_{i|k}) \oplus \mathbb{W}_y \subseteq \mathbb{Y}, \quad (30)$$

where, $\mathbb{Y} = \{y | y \leq [\mu^2, \mu^2, \mu^2, \mu^2]^T\}$.

Remark 3. *Constraints on input magnitude and rate are considered through alternative means. The term for input changes curbs excessive control fluctuations, while the constraint for the friction limit inherently prevents excessive acceleration input or extreme tire slip angle. Stable control results are attained without additional constraints on control amplitude and rate. However, supplementary constraints on actuator performance may be advantageous in more constrained systems.*

Based on the constraints of the original system (30), the constraint for the nominal state is tightened with two components. First, to prevent the constraint's violation due to uncertainty, it is tightened based on the robust invariant set as expressed in (26). Second, additional constraint tightening for the time-varying model is performed to ensure recursive feasibility. This method was developed and inspired by the recursive formulation of previous studies [39], [40]. More details on the feasible condition are given in section IV-C.

Constraint tightening of two components is expressed as follows:

$$\bar{\mathbb{Y}}_0 = \mathbb{Y} \ominus \tilde{\mathbb{Y}}_Z ; \bar{\mathbb{Y}}_{i+1} = \bar{\mathbb{Y}}_i \ominus \tilde{\mathbb{Y}}_{\epsilon,i}, \forall i \in \mathbb{N}_0^{N-1}. \quad (31)$$

For the cost function (28a) and tightened constraint (31), the nominal MPC is expressed as an quadratic programming problem $\mathcal{P}(k)$ as follows:

$$\min_{\bar{\mathbf{u}}_k} \sum_{i=0}^{N-1} \bar{x}^T_{i+1|k} Q \bar{x}_{i+1|k} + \Delta\bar{u}^T_{i|k} \bar{R} \Delta\bar{u}_{i|k}, \quad (32a)$$

subject to.

$$\bar{x}_{0|k} = \bar{x}^*_{1|k-1}, \quad (32b)$$

$$\bar{x}_{i+1|k} = A_{i|k}\bar{x}_{i|k} + B_{i|k}\bar{u}_{i|k} + E_{i|k}, \quad (32c)$$

$$\bar{y}_{i|k} = C_{i|k}\bar{x}_{i|k} + F_{i|k} \in \bar{\mathbb{Y}}_i, \forall i \in \mathbb{N}_0^{N-1}, \quad (32d)$$

$$\bar{x}_{N|k} \in \mathbb{X}_f, \quad (32e)$$

where, $\bar{\mathbf{u}}_k = \{\bar{u}_{0|k}, \ldots, \bar{u}_{N-1|k}\}$. By quadratic programming (32), we can get optimal input sequence $\bar{\mathbf{u}}^*_k$ and calculate optimal states $\bar{x}^*_{i|k}$ through (21). The optimal nominal input $\bar{u}^*_{0|k}$ is applied as the feedforward input of the robust MPC (i.e. $\bar{u}(k) = \bar{u}^*_{0|k}$). Finally, according to the control law (22), the optimal nominal input is applied with the auxiliary feedback input.

B. Multi-Point Linearization

The error resulting from linearization (16) decreases as the linearization points $x_{lin,i|k}$ and $u_{lin,i|k}$ become more similar to the values of $x_o(k+i)$ and $u_o(k+i)$ at which the model prediction is made. This is because the higher-order terms of Taylor's expansion cause larger errors as the linearization points move further away from the points of interest [41]. Therefore, it is important to select $x_{lin,i|k}$ and $u_{lin,i|k}$ to be as similar as possible to $x_o(k+i)$ and $u_o(k+i)$, respectively, in order to minimize the linearization error.

At the k-th step, the values that best represent the future behaviors are $\bar{x}_{o,i+1|k-1}$ and $\bar{u}_{o,i+1|k-1}$. In this study, the nonlinear model is linearized with respect to these values, and it is expressed as follows:

$$\begin{aligned}
A_{o,i|k} =& \nabla_x f_k(x,u)|^{\bar{x}_{o,i+1|k-1}}_{\bar{u}_{o,i+1|k-1}}, B_{o,i|k} = \nabla_u f_k(x,u)|^{\bar{x}_{o,i+1|k-1}}_{\bar{u}_{o,i+1|k-1}},\\
E_{o,i|k} =& f_k(\bar{x}_{o,i+1|k-1}, \bar{u}_{o,i+1|k-1})\\
&- A_{o,i|k}\bar{x}_{o,i+1|k-1} - B_{o,i|k}\bar{u}_{o,i+1|k-1},\\
C_{o,i|k} =& \nabla_x g_k(x,u)|^{\bar{x}_{o,i+1|k-1}}_{\bar{u}_{o,i+1|k-1}}, D_{o,i|k} = \nabla_u g_k(x,u)|^{\bar{x}_{o,i+1|k-1}}_{\bar{u}_{o,i+1|k-1}},\\
F_{o,i|k} =& g_k(\bar{x}_{o,i+1|k-1}, \bar{u}_{o,i+1|k-1})\\
&- C_{o,i|k}\bar{x}_{o,i+1|k-1} - D_{o,i|k}\bar{u}_{o,i+1|k-1},
\end{aligned} \quad (33)$$

where, $\bar{x}_{o,i|k} = [I_6, O_{6\times 8}]\bar{x}_{i|k}$, $\bar{u}_{o,i|k} = [O_{2\times 6}, I_2, O_{2\times 6}]\bar{x}_{i|k}$.

The multi-point linearized model (33) considers the nonlinearity of the model as much as possible, even though the computational burden is dramatically reduced by using the linear model.

C. Recursive Feasibility with Tightened Constraints

In this section, we present and prove the conditions for ensuring the recursive feasibility of $\mathcal{P}(k)$ in (32) that defines the nominal MPC. The recursive feasibility is a property that shows that a solution to the optimization problem must exist. Specifically, this means that if $\mathcal{P}(k)$ is feasible, then $\mathcal{P}(k+1)$ is necessarily feasible. This property is proven by finding a

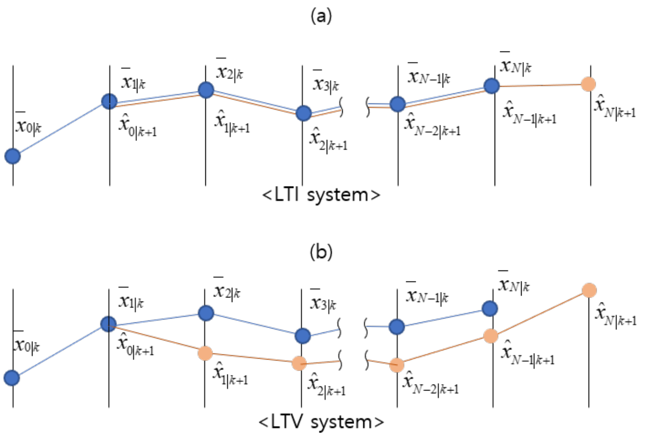

Figure 4. The difference in state prediction for candidate control input

candidate solution that satisfies constraints (32b)-(32e) in the (k+1)-th step when $\mathcal{P}(k)$ is feasible.

For the LTI system, the (k+1)-th candidate input $\hat{u}_{i|k+1}$ is configured to be the same as the optimal input $\bar{u}^*_{i|k}$ (i.e. $\hat{u}_{i|k+1} = \bar{u}^*_{i+1|k}, \forall i \in \mathbb{N}_0^{N-2}$). Since the system is invariant, state predictions of candidate solution $\hat{x}_{i|k+1}$ have the same trajectory with the k-th optimal states (i.e. $\hat{x}_{i|k+1} = \bar{x}^*_{i+1|k}, \forall i \in \mathbb{N}_0^{N-1}$) as shown in Figure 4(a). Therefore, recursive feasibility is proven only with the condition for the terminal constraint X_f, and it has been introduced in various literature [28], [29], [42], [43]. However, the multi-point linearized model is time-varying, so it has a different state trajectory for the same input in the k-th step as shown in Figure 4(b). The (k+1)-th candidate state trajectory is calculated through the following model.

$$\begin{aligned}\hat{x}_{i+1|k+1} &= A_{i|k+1}\hat{x}_{i|k+1} + B_{i|k+1}\hat{u}_{i|k+1} + E_{i|k+1},\\ \hat{y}_{i|k+1} &= C_{i|k+1}\hat{x}_{i|k+1} + F_{i|k+1}.\end{aligned} \tag{34}$$

To avoid the infeasible situation due to model change, a tightened constraint to ensure the LTV system's feasibility was introduced in [39], [40]. We develop the feasibility condition in which the time-varying output function (20) is additionally considered in the form of [40].

The candidate control input can be set as follows:

$$\begin{aligned}&\hat{u}_{i|k+1} = \bar{u}^*_{i+1|k} + \hat{K}_{i|k+1}(\hat{x}_{i|k+1} - \bar{x}^*_{i+1|k}), \forall i \in \mathbb{N}_0^{N-2},\\ &\hat{u}_{N-1|k+1} = \tilde{K}_{N-1|k+1}\hat{x}_{N-1|k+1}.\end{aligned} \tag{35}$$

From this control law, the following lemma is derived.

Lemma IV.1. *The output trajectory for the candidate control law (35) satisfies the following relation:*

$$\begin{aligned}\hat{x}_{i|k+1} &= \bar{x}^*_{i+1|k} + \gamma_{i+1|k}\\ \hat{y}_{i|k+1} &= \bar{y}^*_{i+1|k} + C_{i|k+1}\gamma_{i+1|k} + \epsilon_{g,i+1|k}, \forall i \in \mathbb{N}_0^{N-1},\end{aligned} \tag{36}$$

where,

$$\begin{aligned}\gamma_{1|k} &= O,\\ \gamma_{i+1|k} &= A^{\hat{K}}_{i-1|k+1}\gamma_{i|k} + \epsilon_{f,i|k}, \forall i \in \mathbb{N}_1^{N-1},\end{aligned} \tag{37}$$

$A^{\hat{K}}_{i|k} = A_{i|k} + B_{i|k}\hat{K}_{i|k}$, *and the differences between the nominal states and the nominal outputs due to model variance are as follows:*

$$\begin{aligned}\epsilon_{f,i|k} &= (A_{i-1|k+1} - A_{i|k})\bar{x}^*_{i|k} + (E_{i-1|k+1} - E_{i|k}),\\ \epsilon_{g,i|k} &= (C_{i-1|k+1} - C_{i|k})\bar{x}^*_{i|k} + (F_{i-1|k+1} - F_{i|k}),\\ &\qquad\qquad \forall i \in \mathbb{N}_1^{N-1},\\ \epsilon_{g,N|k} &= (C_{N-1|k+1} - C_{N-1|k})\bar{x}^*_{N|k} + (F_{N-1|k+1} - F_{N-1|k}).\end{aligned} \tag{38}$$

The detailed proof of Lemma IV.1 is in Appendix A.

The sets including the error states of (37) and (38) are defined as follows $\forall A \in \mathbb{A}, \forall E \in \mathbb{E}, \forall C \in \mathbb{C}, \forall F \in \mathbb{F}$:

$$\begin{aligned}&\epsilon_{f,i|k} \in \eta_{f,i} = \bigcup_k \epsilon_{f,i|k}, \forall i \in \mathbb{N}_1^{N-1},\\ &\epsilon_{g,i|k} \in \eta_{g,i} = \bigcup_k \epsilon_{g,i|k}, \forall i \in \mathbb{N}_1^{N},\\ &\gamma_{1|k} \in \Gamma_1 = O,\\ &\gamma_{i+1|k} \in \Gamma_{i+1} = \bigcup_k A^{\hat{K}}_{i|k}\Gamma_i \oplus \eta_{f,i}, \forall i \in \mathbb{N}_1^{N-1},\\ &C_{0|k+1}\gamma_{1|k} \in \Theta_1 = O,\\ &C_{i|k+1}\gamma_{i+1|k} \in \Theta_{i+1} = \bigcup_k C_{i+1|k}\left(A^{\hat{K}}_{i|k}\Gamma_i \oplus \eta_{f,i}\right), \forall i \in \mathbb{N}_1^{N-1}.\end{aligned} \tag{39}$$

The constraint tightening that guarantees recursive feasibility can be determined as follows:

$$\tilde{\mathbb{Y}}_{\epsilon,i} = \Theta_{i+1} \oplus \eta_{g,i+1}. \tag{40}$$

Moreover, the following assumptions are made for the terminal state:

Assumption IV.2. *There exists a control law $\tilde{K}_{N-1|k+1}$ such that the terminal state constraint $\mathbb{X}_f$ satisfies the following properties:*

$$\begin{aligned}&A^{\tilde{K}}_{N-1|k}(\mathbb{X}_f \oplus \Gamma_N) + E_{N-1|k} \subseteq \mathbb{X}_f,\\ &C_{N-1|k}\mathbb{X}_f + F_{N-1|k} \in \bar{\mathbb{Y}}_N.\end{aligned} \tag{41}$$

Based on the constraint tightening (31), (40) and Assumption IV.2, we can state:

Proposition IV.3. *If the optimization for the initial state $\mathcal{P}(0)$ is feasible, subsequent control behaviors with tightened constraints (31),(40) are feasible, i.e. $\mathcal{P}(k)$ is feasible.*

The proof of Proposition IV.3 is in Appendix B.

Remark 4. *Unlike the control input (22) used as a system input, the candidate control input (35) is only used to find a feasible solution but is not used as a system input. The feedback input added in (35) makes $A^{\hat{K}}_{i|k}$ stable and attenuates the state error occurring in the LTV system. This feedback input reduces the size of recursive constraint tightening $\tilde{\mathbb{Y}}_{\epsilon,i}$, avoiding overly conservative control.*

Lemma IV.1 and Proposition IV.3 are developed from the form described in [40]. In this study, the effective change compared to [40] is that by dealing with the effect of the

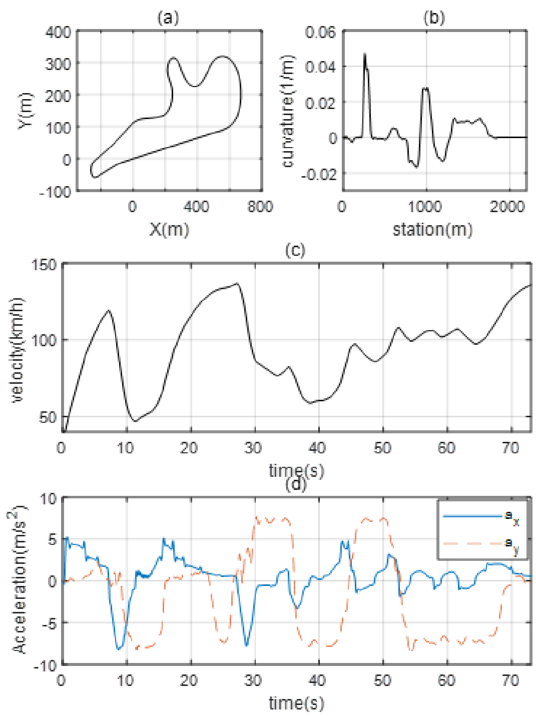

Figure 5. Driving data for constraint tightening

uncertainty $\omega(k)$ of the actual state through (22) and (26). Therefore, the initial state of optimization $\bar{x}_{0|k}$ is set to the nominal state of the previous step $\bar{x}^*_{1|k-1}$ as in (32b), not the actual state $x(k)$. This difference results in two practical benefits in our controller. First, recursive constraint tightening (40) can be calculated off-line since it is unnecessary to consider the effect of time-varying uncertainty $\omega(k)$ in a nominal system. Therefore, there is no increase in real-time calculations for constraint tightening. Also, since the initial state of nominal MPC starts from the nominal state of the previous step, the model change due to multi-point linearization (38) can be reduced. If the actual state $x(k)$ is used as an initial value, since the model is linearized for the state containing $\omega(k)$, the magnitude of the model change becomes larger. As the result, the constraint must be tightened even more to account for this. Therefore, if the initial state is defined as the nominal state of the previous step as in (32b), less conservative control is possible by reducing the constraint tightening proportional to the size of the model variation.

D. Practical Calculation of Tightened Constraints based on Driving Data

This section introduces a practical method for calculating the tightened constraint. Theoretically, the calculation of constraint tightening (31) for a time-varying system should be done $\forall A(k) \in \mathbb{A}, \forall B(k) \in \mathbb{B}, \forall E(k) \in \mathbb{E}, \forall C(k) \in \mathbb{C}$, and $\forall F(k) \in \mathbb{F}$ as described above. However, from a practical point of view, it can be overly conservatively tightened by considering cases that cannot actually occur. Therefore, in this

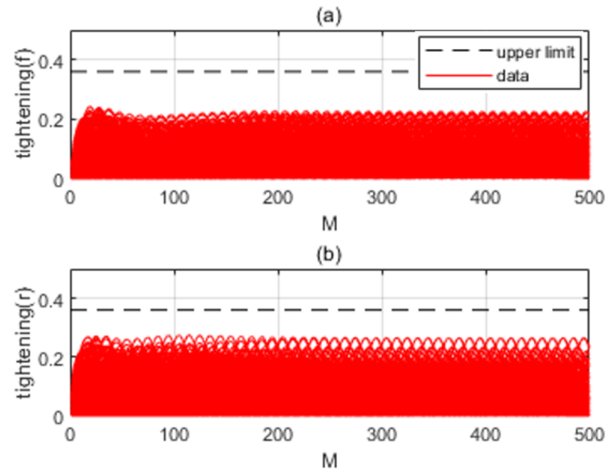

Figure 6. Calculation of $\tilde{\mathbb{Y}}_Z$

section, the impact of uncertainty that can occur based on numerous driving data is analyzed, and a tightened constraint is defined based on this.

1) Calculation of $\tilde{\mathbb{Y}}_Z$: The robust positive invariant set Z and the resulting constraint tightening $\tilde{\mathbb{Y}}_Z$ are calculated as follows instead of (24) and (27).

$$Z \cong \bigcup_k \lim_{M\to\infty} A^K(k+M-1)\Big(\cdots \big(A^K(k+1)\mathbb{W} \oplus \mathbb{W}\big)\cdots\Big) \oplus \mathbb{W}, \tag{42}$$

$$\tilde{\mathbb{Y}}_Z \supseteq \bigcup_k \lim_{M\to\infty} \mathbb{W}_y \oplus C(k+M)[A^K(k+M-1)\Big(\cdots \big(A^K(k+1)\mathbb{W} \oplus \mathbb{W}\big)\cdots\Big) \oplus \mathbb{W}]. \tag{43}$$

The uncertainty magnitudes $\omega(k)$, $\omega_y(k)$ at each step in the data is defined as the difference between the measured and model-calculated values, and is calculated via equations (19) and (20). The model for this calculation is constructed by linearizing based on the actual occurring state and inputs. From this, $\mathbb{W}$ and $\mathbb{W}_y$ are defined by considering all the combinations of maximum and minimum $\omega(k)$ and $\omega_y(k)$ in the data for each state. Thus, the calculations of Z and $\tilde{\mathbb{Y}}_Z$ take into account both the maximum and minimum values of uncertainty for each state. And the control gain $K(k)$ is defined as the linear quadratic regulator (LQR) for matrix pair $(A(k), B(k))$. Using the Matlab function $\text{dlqr}(A(k), B(k), Q_{LQR}, R_{LQR})$, it is calculated in real-time for the cost matrices defined as follows:

$$\begin{aligned} Q_{LQR} &= \text{diag}(0.1, 1, 1, 0.01, 1, 0.1, O_{6\times 6}), \\ R_{LQR} &= \text{diag}(5000, 10) \end{aligned} \tag{44}$$

This calculation can avoid conservative calculations for unrealistic system model sequences. Nevertheless, to consider as many different cases as possible, the analysis was based on extreme driving data of the racing circuit. The driving data used in this study was collected from a circuit driving experiment conducted with a specific target vehicle. The

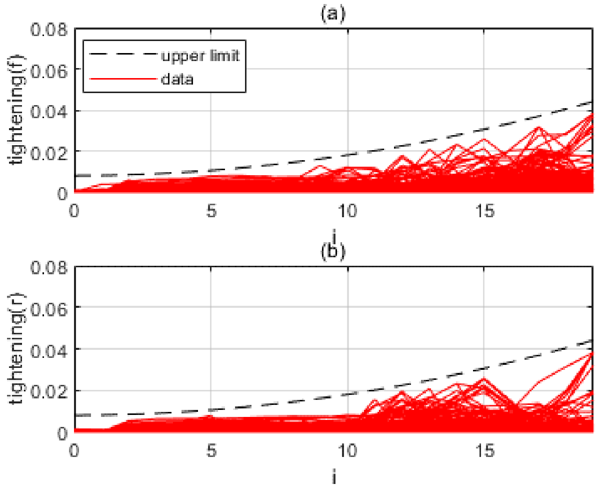

Figure 7. Calculation of $\tilde{\mathbb{Y}}_{\epsilon,i}$

driving data, including the data shown in Figure 5, has a distance of about 10 km and an acceleration range of about 0.9 g. The term on the right of (43) calculated based on driving data is represented by the red lines in Figure 6. The upper bound of constraint tightening including all of them is defined as follow:

$$\tilde{\mathbb{Y}}_Z = \{y|y \leq [0.36, 0.36, 0.36, 0.36]^T\} \tag{45}$$

The tightened constraint of the first nominal output by (31) is as follow:

$$\bar{\mathbb{Y}}_0 = \mathbb{Y} \ominus \tilde{\mathbb{Y}}_Z = \{y|y \leq [0.64, 0.64, 0.64, 0.64]^T\} \tag{46}$$

Therefore, for all wheels, as long as the square of the normalized tire force of the nominal system (21) does not exceed 0.64 (i.e. $\bar{F}_n^j < 0.8, \forall j = fl, fr, rl, rr$), it is guaranteed that the normalized tire force of the actual system (19) with uncertainty does not exceed the road friction limit of 1 (i.e. $F_n^j < 1, \forall j = fl, fr, rl, rr$).

2) Calculation of $\tilde{\mathbb{Y}}_{\epsilon,i}$: For the same reason as before, it was calculated based on controlled driving data to prevent unnecessary conservative tightening. The control gain $\hat{K}_{i|k}$ is also an LQR control gain for the matrix pair $(A_{i|k}, B_{i|k})$ and the cost matrices Q_{LQR} and R_{LQR}. The impact of model variations on the output vector for controlled driving data is expressed as follows and represented as shown in Figure7 (red line).

$$\hat{y}_{i|k+1} - \bar{y}^*_{i+1|k} = C_{i|k+1}\gamma_{i+1|k} + \epsilon_{g,i+1|k}, \forall i \in \mathbb{N}_0^{N-1}, \tag{47}$$

Therefore, $\tilde{\mathbb{Y}}_{\epsilon,i}$ is defined (40) as an upper bound that encompasses all effects caused by model variance in the driving data. In this study, the upper bound is defined as a second-order polynomial for the prediction step, which has been tuned and expressed as follows, and represented by a dashed black line in Figure 7.

$$\tilde{\mathbb{Y}}_{\epsilon,i} = \{y|y \leq (0.0001(i)^2 + 0.008)[1,1,1,1]^T\}, \forall i \in \mathbb{N}_0^{19} \tag{48}$$

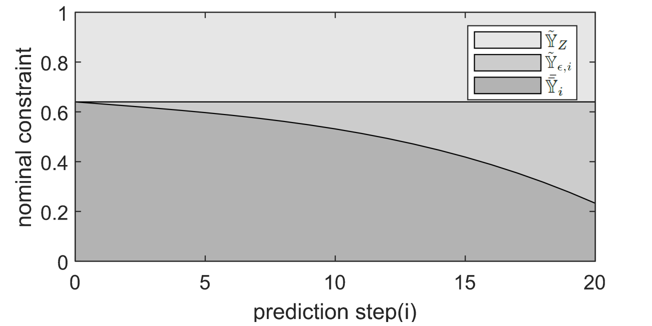

Figure 8. Calculation of $\bar{\mathbb{Y}}_i$: The relationship between the size of two types of constraint tightening and the tightened constraint

Constraint tightening $\tilde{\mathbb{Y}}_{\epsilon,i}$ inductively tightens the nominal constraint $\bar{\mathbb{Y}}_i$ with respect to the prediction step according to equation (31). The final tightened constraint is expressed as follows and is depicted in Figure 8:

$$\begin{aligned} &\bar{\mathbb{Y}}_{i+1} = \bar{\mathbb{Y}}_i \ominus \tilde{\mathbb{Y}}_{\epsilon,i} \\ &= \{y|y \leq \bar{y}_{i+1}[1,1,1,1]^T\}, \forall i \in \mathbb{N}_0^{19}, \\ &= \{y|y \leq (\bar{y}_i - 0.0001(i)^2 - 0.008)[1,1,1,1]^T\}, \forall i \in \mathbb{N}_0^{19}, \end{aligned} \tag{49}$$

where, $\bar{y}_0 = 0.64$.

Finally, the calculated tightened nominal constraint is employed as the constraint for the proposed nominal controller. Through this, the controller ensures compliance with constraints despite any model uncertainty that may arise within the driving data and guarantees feasibility regardless of model changes, due to the constraint tightening (47) in the prediction step.

While the proposed constraint tightening method has the advantage of being less conservative, its limitation lies in only considering the uncertainties present in the data. If the calculations lack a sufficient amount of diverse data, unintended control actions may result from excessive uncertainty not represented in the data or variance in the prediction model. It is important to note that under aggressive driving conditions, such as high-speed and high-acceleration scenarios, the model's uncertainty increases, as does the variance in the prediction model due to changes in vehicle behavior. In this study, we computed constraint tightening using a comprehensive and diverse dataset, encompassing severe driving data from high-speed and high-acceleration scenarios on high-friction road surfaces. Consequently, the method effectively covers a broad spectrum of driving conditions on high-friction road surfaces, including extreme situations. Furthermore, it is anticipated that expanding data collection and calculations will allow the approach to address conditions not yet covered in the data, such as low-friction road surfaces.

E. Effects of Tightened Constraints on the Linearization Process

Constraint tightening not only increases the robustness of the controller, but is also effective against problems in the lin-

Table I
MODEL PARAMETERS

Parameter	Value	Parameter	Value
m	1854 kg	μ	1
I_z	3966 kg·m^2	θ_y	0.165
b	0.815m	h_{cg}	0.55
l_f, l_r	1.40, 1.61 m	σ_f, σ_r	0.178, 0.189
c_d	0.504 N·s^2/m^2	$\tau_{l,\delta}, \tau_{l,a_x}$	0.1, 0.01 s
λ	0.7	$\tau_{d\delta}, \tau_{d,a_x}$	0.2, 0.2 s

Table II
CONTROL PARAMETERS

Parameter	Value
T_s	0.1 s
N	20
q_{e_y}	10
q_{a_x}	0.005
$\bar{R}$	diag(30, 0.001)

earization of nonlinear tire models. Cornering stiffness of the nonlinear tire model decreases rapidly when tire forces enter the nonlinear region during extreme lateral behavior, leading to a quick increase in linearization errors when linearizing a vehicle model that uses a nonlinear tire model.

If the linearization error increases significantly, controllers using these models may experience poor control performance, as the difference between the actual vehicle behavior and the nominal model becomes larger. For example, if the nominal model predicts a higher slip angle than the actual one, excessive steering input may occur, resulting in unstable vehicle behavior. Conversely, if the nominal model predicts a lower slip angle than required, insufficient steering input may occur.

However, the proposed controller effectively mitigates these problems in the nonlinear regions by tightening the constraints. By enforcing the tire force constraint, it ensures that the tire force generation in the nominal model does not exceed 80% of the actual road friction. As a result, the slip angle in the nominal model does not behave in the region where the cornering stiffness converges to zero but in a less nonlinear region. Therefore, the model benefits greatly from a linearization perspective, contributing to reducing the linearization error. In this case, if the actual slip angle is larger than the nominal model due to uncertainty, the nominal model may have a higher lateral error due to less coordination force resulting from a larger estimate of cornering stiffness than the actual value. However, the unstable behavior of the vehicle in the opposite case can be effectively suppressed.

Overall, these constraints and optimizations minimize model errors in excessively nonlinear regions, leading to more stable and accurate results in vehicle steering control. This helps to improve safety and performance.

V. SIMULATION RESULT

This section introduces the simulation results of the controller previously designed in section IV. A vehicle simulator, Carsim, was utilized for the simulation, and the controller was designed using Matlab simulink. The nominal MPC

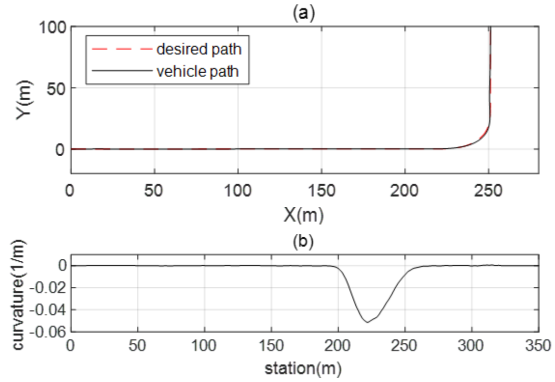

Figure 9. Simulation result : Desired path

quadratic programming calculations (32) and the calculations for the linearized model (33) were done using the functions quadprog() and jacobian() in Matlab, respectively. Specifically, the linearization model was defined offline in ”symbolic(sym)” form and only substitution was performed during control, making it effective for real-time performance. The vehicle used in the simulation consists of the same parameters as the test vehicle to be introduced in section VI, which is presented in Table I. Also, the control parameters are as in Table II. The simulations were performed for the scenario of entering at high speed (95km/h) on the curved road shown in Figure 9. In section V-A, we demonstrate the operating principles and control performance of the proposed controller, while section V-B and V-C discusses the effects of constraint tightening.

A. Operating Principle

As a result of the simulation, the control input was generated as shown in Figure 10 (a), (b), and the nominal MPC input and the feedback input are commanded together. The commanded inputs were applied to the vehicle under the influence of delays and lags of the actuators. As shown in Figure 10 (c), (d), the vehicle's speed was significantly reduced before turning, and the lateral distance error occurred within 0.5m. Also, due to proper braking, it can be seen that the tire force of each wheel shown in Figure 11 occurred within the friction limit during control.

The braking input was not generated from the additional speed planner but rather from the influence of the constraint of the controller shown in Figure 12. The cost function of the controller focuses only on reducing lateral error regardless of speed. However, the brake input was automatically generated to avoid excessive lateral force due to tire force constraints at high speeds.

In this scenario, the load on the left wheel is reduced when turning, so it may become unstable when braking and steering are performed together. Because the proposed controller considers the force of each wheel, the constraint of the left tire forces was activated and is validated by the blue dots in Figure 12. Since constraint is guaranteed by (49), the controller was always feasible during simulation. Without this constraint tightening, the optimization solution did not exist at some point, and the simulation stopped.

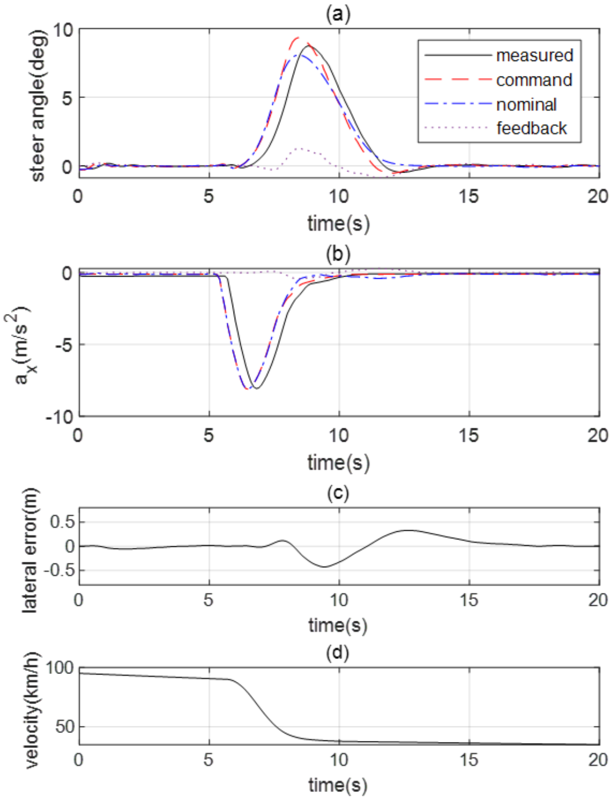

Figure 10. Simulation result : Inputs and states

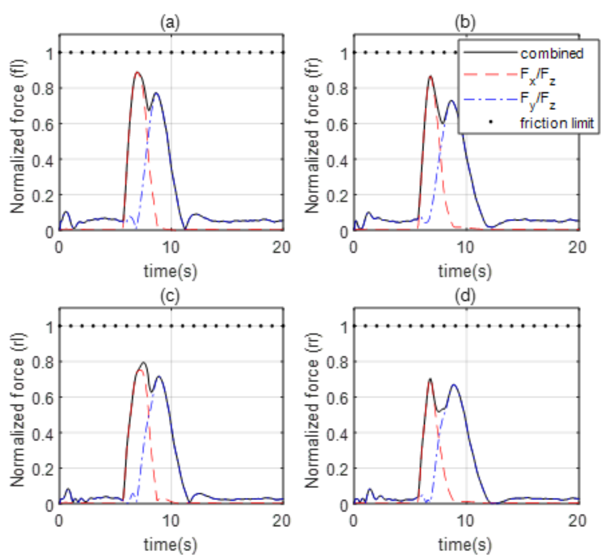

Figure 11. Simulation result : Tire forces

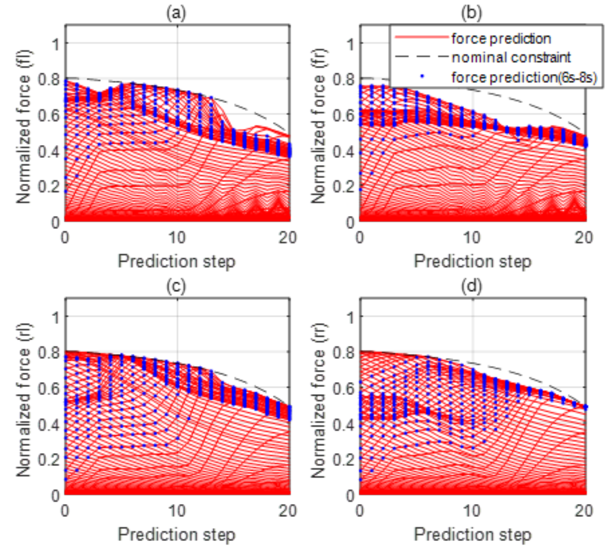

Figure 12. Simulation result : Constraint satisfaction

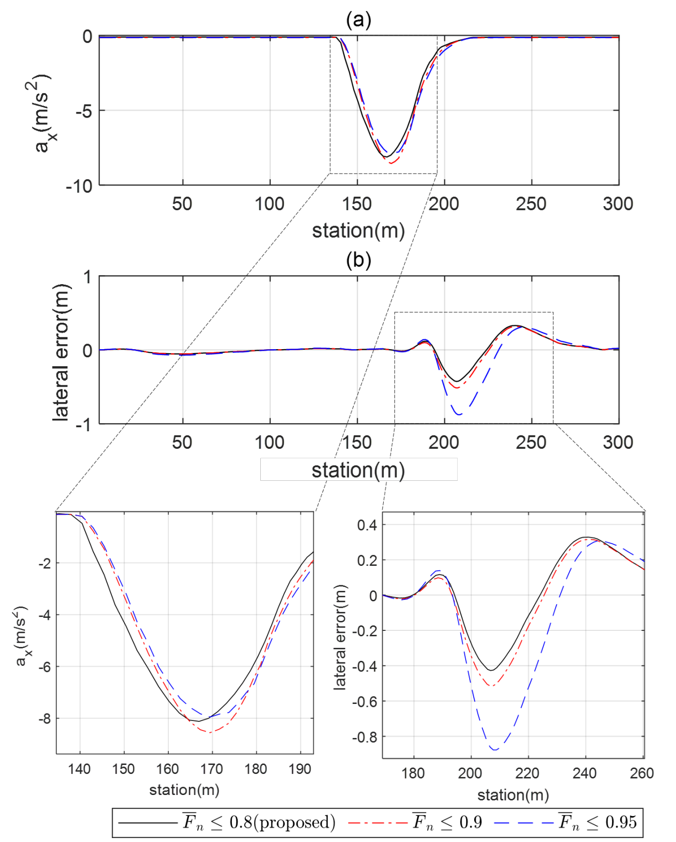

Figure 13. The effect of insufficient $\tilde{\mathbb{Y}}_Z$: a_x and e_y

B. The Effect of $\tilde{\mathbb{Y}}_Z$

In this simulation, the effect of constraint tightening $\tilde{\mathbb{Y}}_Z$ based on robust positive invariant sets for robustness against model uncertainty is analyzed. The result from the data-driven constraint tightening $\tilde{\mathbb{Y}}_Z$ is defined as $\bar{\mathbb{Y}}_0 = \{y|y \leq [0.64, 0.64, 0.64, 0.64]^T\}$ (i.e. $\bar{F}_n^j < 0.8, \forall j = fl, fr, rl, rr$) as expressed in (46). However, if the data used to calculate $\tilde{\mathbb{Y}}_Z$ is not sufficiently representative of severe driving situations, a smaller tightening value may be calculated. As a result, the constraints of the nominal MPC are applied less conservatively. Therefore, in this simulation, we compare the results for less conservative tightening with $\bar{\mathbb{Y}}_0 = \{y|y \leq (0.9)^2[1,1,1,1]^T\}$ and $\bar{\mathbb{Y}}_0 = \{y|y \leq (0.95)^2[1,1,1,1]^T\}$ as

This article has been accepted for publication in IEEE Transactions on Vehicular Technology. This is the author's version which has not been fully edited and content may change prior to final publication. Citation information: DOI 10.1109/TVT.2023.3292616

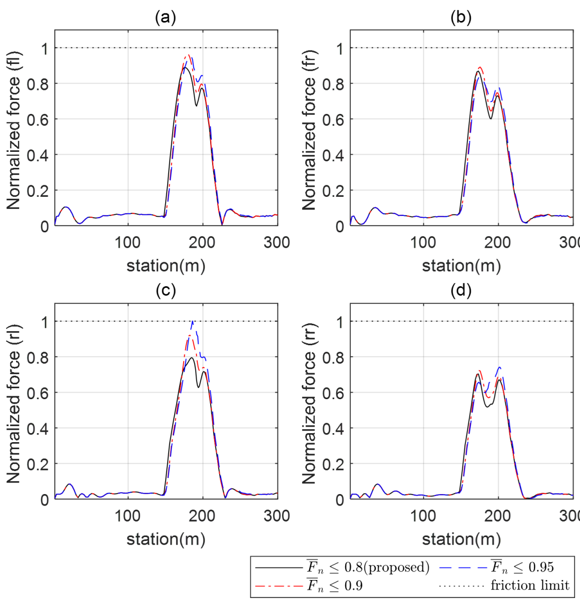

Figure 14. The effect of insufficient $\tilde{\mathbb{Y}}_Z$: Tire forces

shown in Figures 13 and 14. The simulation scenario is the same as V-A.

When the nominal tire force limit was set to 0.9, the behavior was very similar to the proposed result. Successful control was achieved even with less conservative constraints because the calculation of $\tilde{\mathbb{Y}}_Z$ was based on the worst-case scenario of severe driving data in Figure 5. Therefore, the result set to 0.9 shows that the proposed data-driven constraint tightening is not overfitting for this particular scenario. It should also be recognized that the result is set less conservatively than the data-driven calculation and therefore may not always show successful control in other environments.

On the other hand, when the nominal tire force constraint was slightly increased to 0.95, the normalized tire force of the left rear wheel shown in Figure 14(c) violated the actual tire force constraint due to the effect of uncertainty. As a result, the lateral error in Figure 13(b) was inaccurate at 0.87 m, which is about twice as large as the behavior under the proposed constraint.

As a result, through this simulation result, it can be confirmed that the driving data-based constraint tightening is sufficiently effective against the occurrence of uncertainty.

C. The Effect of $\tilde{\mathbb{Y}}_{\epsilon,i}$

In this simulation, the effect of constraint tightening on the feasibility of a controller is analyzed. The size of the proposed tightening $\tilde{\mathbb{Y}}_{\epsilon,i}$ creates a margin for model variations, ensuring that the nominal MPC always has a solution that satisfies the constraints. To verify the effectiveness of this method, the performance of the controller is compared with various sizes of $\tilde{\mathbb{Y}}_{\epsilon,i}$. Table III and Figure15 show the size of the proposed sequential tightening and the maximum calculation time of each control.

In Case 2, although the size of sequential tightening is less conservative than the proposed constraint, the controller is still always feasible and the behavior is similar to Case 1. However, the calculation time shown in Figure15 and in Table III increases at a specific section due to a reduction in the number of constraint-satisfying solutions. Through this, it can be seen that the sequential tightening not only guarantees feasibility, but also helps to improve the calculation speed of constrained optimization by increasing the size of the feasible set. In Case 3, the simulation stopped at 167m without finding a solution that satisfies the constraints due to model variance, as indicated by the diverging calculation time shown in Figure15.

Overall, through this simulation result, it can be confirmed that the definition and calculation of sequential tightening proposed in this dissertation is effective in ensuring feasibility for model change.

Table III
THE SIZE OF SEQUENTIAL TIGHTENING AND CALCULATION TIME

Method	$\tilde{\mathbb{Y}}_{\epsilon,i}$	Max Comp. time(ms)
Case 1 (Proposed)	$0.0001(i)^2 + 0.008$	9.7
Case 2	$0.0001(i)^2 + 0.004$	21.15
Case 3	$0.0001(i)^2 + 0.002$	infeasible

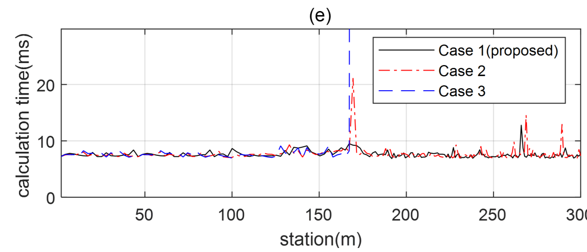

Figure 15. The effect of constraint tightening ($\tilde{\mathbb{Y}}_{\epsilon,i}$) : Calculation time

VI. EXPERIMENT RESULT

In this section, we show the effectiveness of the proposed controller through vehicle test results. Vehicle tests are conducted on a curved road and a single lane change (SLC) path to confirm lane-keeping and collision avoidance performance in extreme situations.

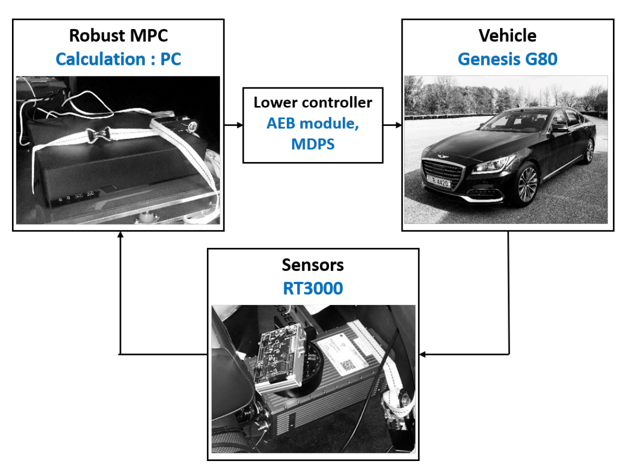

Figure 16. Experimental setup

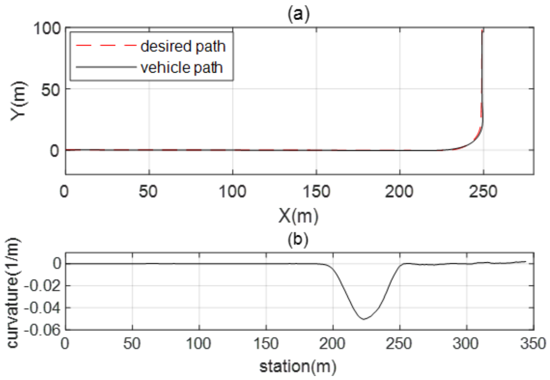

Figure 17. Experimental result (curved road) : Desired path

A. Experimental Setup

Figure 16 shows a simplified experimental setup. The Hyundai Genesis DH, an E-class sedan, was used as the test vehicle, and the vehicle's states are measured through the RT3000 mounted on the vehicle CG. The controller was run via Matlab on a personal computer with AMD Ryzen 9 3900X and 64GB RAM. Calculations for each element were performed in the same way as in the simulation. Steering angle input and braking input were respectively actuated by a motor-driven power steering (MDPS) system and autonomous emergency braking (AEB) actuator. Sensors, PCs, and actuators communicate through Robot Operating System (ROS) communication and CAN. Predefined path information was used as the desired path of path tracking.

B. Curved Road

The curved road scenario shown in Figure 17 is similar to the simulation and is the best scenario to check the performance of the proposed controller. Proper turning and braking are prominently expressed when approaching a sharp corner at high speed. Figure 18(a),(b) shows the inputs of steering and braking, consisting of nominal MPC input and feedback input. In particular, since the actuator's performance was considered, unnecessary chattering rarely occurs. In addition, this controller has a small amount of computation in real-time due to the utilization of quadratic programming using the linearized model and the off-line computation of constraint tightening. The calculation time per step of the controller shown in Figure 18(c) is less than 2ms, which is very generous compared to the time interval of 100ms.

The vehicle motions are shown in Figure 18(d),(e). The lateral distance error occurred within 0.52m, and the vehicle speed was greatly reduced from the maximum speed of about 90km/h to about 40km/h. Unfortunately, measuring the tire forces was impossible, so the effectiveness of the controller was confirmed through the longitudinal/lateral acceleration shown in Figure 18(f). After the vehicle brakes up to 7.5, mixed acceleration in the longitudinal/transverse direction occurred. After braking almost disappeared, a lateral acceleration of up to 8.7 occurred. When all four wheels simultaneously generate maximum force, a vehicle acceleration of 1g (i.e. 9.81m/s^2), equal to the road friction limit, can occur. Therefore, it can be inferred that all tire forces are utilized almost to the maximum in a stable area where the road friction limit is not exceeded all the time. Therefore, it is confirmed that the amount of braking of this controller is not excessive or insufficient, and it shows stable turning performance even in a situation where combined acceleration occurs through the steering control considered together.

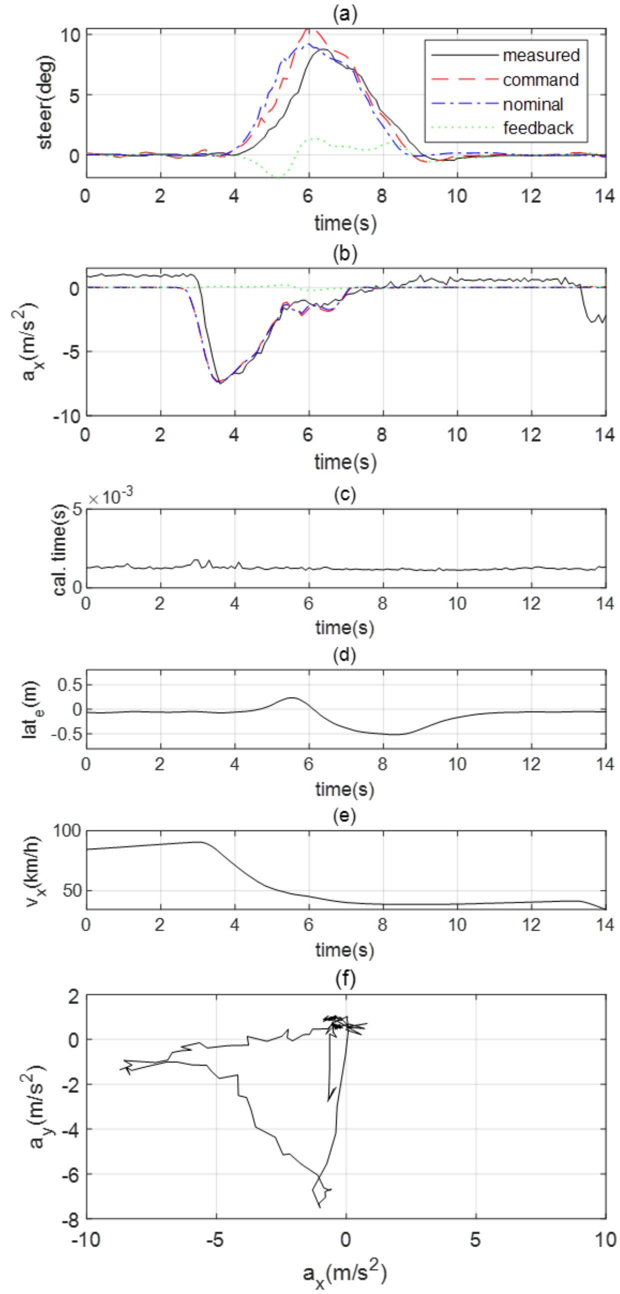

Figure 18. Experimental result (curved road) : Inputs and states

C. Single Lane Change

The SLC path is shown in Figure 19. A vehicle test on this path was performed to validate the performance of the proposed controller in obstacle avoidance behavior. In particular,

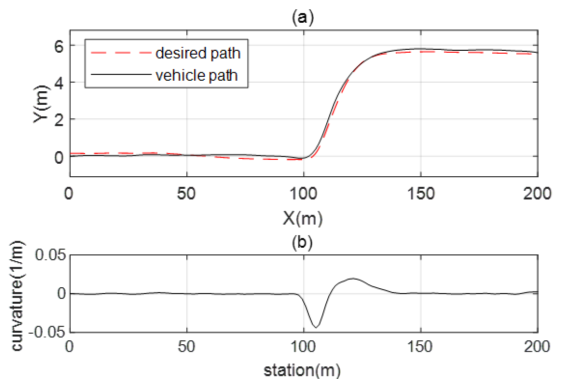

Figure 19. Experimental result (SLC) : Desired path

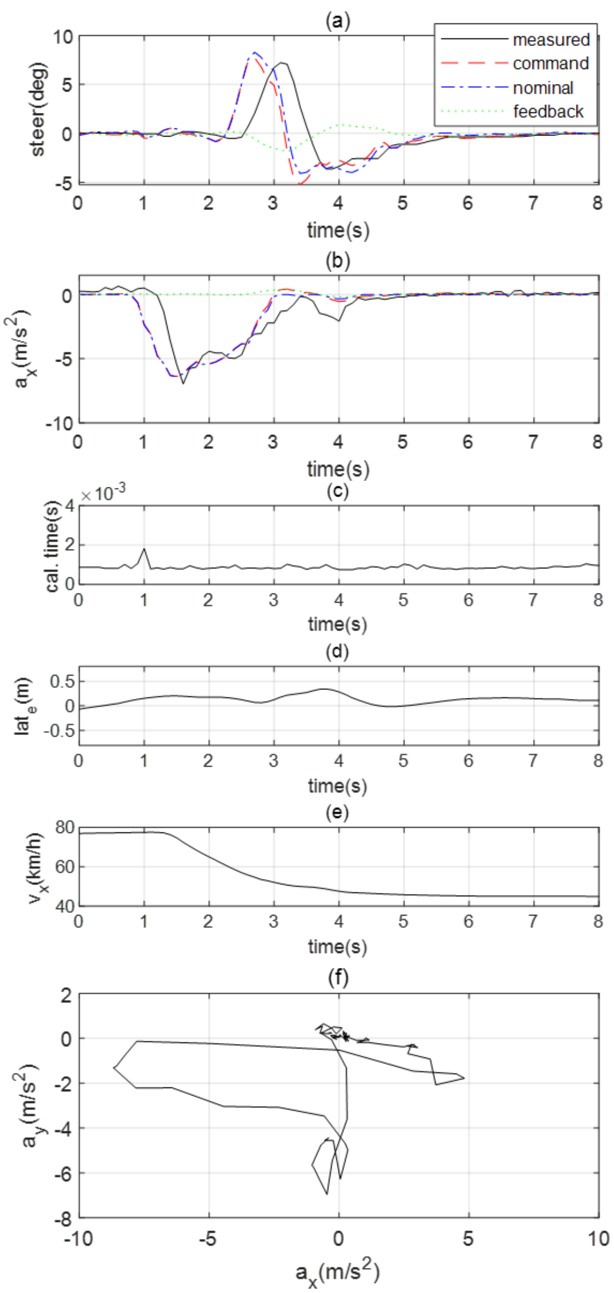

Figure 20. Experimental result (SLC) : Inputs and states

bold steering control is required because it requires a lateral movement as large as about 5 m for a longitudinal distance of less than 30 m. Therefore, it is suitable for verifying control performance for transient situations. Figure 20(a-c) shows the controller's input, and the computation time is less than 2 ms, which shows a slight computational burden as in the curved road scenario.

The vehicle motions are shown in Figure 20(d),(e). Due to proper steering control, a maximum lateral error of 0.34m occurred, and the vehicle speed was reduced from a high speed of about 77km/h to about 45km/h for stable turning. The acceleration result shows that braking was applied before turning left, and the braking input almost disappeared when significant lateral acceleration was required. As it can be seen that almost no braking occurred just before the right turn, it can be confirmed that the proposed controller does not generate unnecessary braking input when low lateral acceleration is expected.

VII. Conclusion and Future Works

In this paper, we proposed a tube MPC-based steering and braking controller for path tracking in extreme driving situations. Through the friction limit constraint of each tire, the vehicle can stably follow a path even in an extreme driving situation. In particular, since the model uncertainty can cause fatal accidents in such a driving situation, precise analysis and consideration of the robustness of the controller were accompanied. The proposed multi-point linearization method reduces the linearization error while maintaining the computational efficiency of the linear model. Moreover, a vehicle model considering input delays and lags was used for control. The proposed tube MPC-based controller prevents constraint violation due to uncertainty and guarantees feasibility. The conditions for securing feasibility were explained and proven through lemma and proposition. The tightened constraint of the controller was calculated based on driving data. The performance of the proposed algorithm was verified through simulations and experiments. As a result, the vehicle performed stable and accurate path tracking without violating friction constraints. In particular, the vehicle braked to a stable speed range without a separate speed planner and behaved stably even when performing longitudinal/lateral combined motion.

The proposed methodology in this paper can be further enhanced through the following additional research directions. First, beyond the uncertainty addressed in this study, further analysis of uncertainties, such as sensor errors, localization errors, and delays that may arise from mass-produced vehicles' sensors, as well as additional analysis of vehicle behavior on low friction surfaces, would enable the proposed controller to be applied to a broader range of vehicles and scenarios. To achieve this, additional data collection beyond what was used for constraint tightening calculations in this study is expected to help improve the tightening amount and be sufficient to address these uncertainties. Second, while this paper provided a mathematical proof of feasibility for the proposed system, we plan to conduct further theoretical investigations on the controller's stability. The current control results reliably converge to the desired results within a stable range of tire forces; however, a theoretical stability study can further ensure the stability of the controller. Lastly, we intend to expand the application of the proposed control methodology to not only braking control but also acceleration input through throttle input, broadening its potential uses.

ACKNOWLEDGEMENT

This research was partly supported by the BK21 FOUR Program of the National Research Foundation Korea (NRF) grant funded by the Ministry of Education (MOE), the Technology Innovation Program (20014983, Development of autonomous chassis platform for a modular vehicle) funded By the Ministry of Trade, Industry and Energy (MOTIE, Korea), the National Research Foundation of Korea (NRF) grant funded by the Korea government (MSIP) (No. 2020R1A2B5B01001531), and the grant (21TLRP-C152499-03) from Transportation and Logistics Research Program funded by Ministry of Land, Infrastructure and Transport (MOLIT) of Korea government and Korea Agency for Infrastructure Technology Advancement (KAIA).

APPENDIX A
PROOF OF LEMMA IV.1

Proof. Proving this by induction, for $i = 0$,

$$\begin{aligned}\hat{x}_{0|k+1} &= \bar{x}^*_{1|k} + \gamma_{1|k}, \\ \hat{y}_{0|k+1} &= C_{0|k+1}\hat{x}_{0|k+1} + F_{0|k+1} \\ &= \bar{y}^*_{1|k} + C_{0|k+1}\gamma_{1|k} + \epsilon_{g,1|k}.\end{aligned} \tag{50}$$

Assuming that (36)-(38) hold for i, we need to verify that they hold for $i+1$.

$$\begin{aligned}\hat{x}_{i+1|k+1} &= A_{i|k+1}\hat{x}_{i|k+1} + B_{i|k+1}\hat{u}_{i|k+1} + E_{i|k+1} \\ &= A_{i|k+1}\left(\bar{x}^*_{i+1|k} + \gamma_{i+1|k}\right) + B_{i|k+1}\hat{u}_{i|k} + E_{i|k+1} \\ &= \bar{x}^*_{i+2|k} + A^{\hat{K}}_{i|k+1}\gamma_{i+1|k} + \epsilon_{f,i+1|k}, \\ &= \bar{x}^*_{i+2|k} + \gamma_{i+2|k}, \\ \hat{y}_{i+1|k+1} &= C_{i+1|k+1}\hat{x}_{i+1|k+1} + F_{i+1|k+1} \\ &= C_{i+1|k+1}\left(\bar{x}^*_{i+2|k} + \gamma_{i+2|k}\right) + F_{i+1|k+1}, \\ &= \bar{y}^*_{i+2|k} + C_{i+1|k+1}\gamma_{i+2|k} + \epsilon_{g,i+2|k}.\end{aligned} \tag{51}$$

This finally proves Lemma IV.1 by induction. □

APPENDIX B
PROOF OF PROPOSITIONIV.3

Proof. For recursive feasibility, we want to verify that $\mathcal{P}(k+1)$ is feasible when $\mathcal{P}(k)$ is feasible. This is shown by finding a candidate solution that satisfies constraints (32b)-(32e). (36) was derived to satisfy constraints (32b), (32c).

$$\begin{aligned}\hat{y}_{i|k+1} &= \bar{y}^*_{i+1|k} + C_{i|k+1}\gamma_{i+1|k} + \epsilon_{g,i+1|k} \\ &\in \mathbb{Y}_{i+1} \oplus \Theta_{i+1} \oplus \eta_{g,i+1} \\ &= \bar{\mathbb{Y}}_i \ominus \tilde{\mathbb{Y}}_{\epsilon,i} \oplus \Theta_{i+1} \oplus \eta_{g,i+1} \\ &= \bar{\mathbb{Y}}_i\end{aligned} \tag{52}$$

Therefore, the candidate solution satisfies the constraint (32d). Also, for the terminal state,

$$\begin{aligned}\hat{x}_{N-1|k+1} &= \bar{x}^*_{N|k} + \gamma_{N|k}, \\ &\in \mathbb{X}_f \oplus \Gamma_N.\end{aligned} \tag{53}$$

This relationship, with Assumption IV.2, enables us to show that:

$$\begin{aligned}\hat{x}_{N|k+1} &= A^{\tilde{K}}_{N-1|k+1}\hat{x}_{N-1|k+1} + E_{i|k+1}, \\ &\in A^{\tilde{K}}_{N-1|k+1}\left(\mathbb{X}_f \oplus \Gamma_N\right) + E_{i|k+1}, \\ &\subseteq \mathbb{X}_f.\end{aligned} \tag{54}$$

Therefore, it is proved that the candidate solution (35) is also satisfied with the terminal constraint (32e). Finally, there is a candidate solution (35) for $\mathcal{P}(k+1)$ that satisfies the tightened constraint (32b)-(32e), $\mathcal{P}(k+1)$ is feasible. □

REFERENCES

[1] W. Lim, S. Lee, M. Sunwoo, and K. Jo. Hierarchical trajectory planning of an autonomous car based on the integration of a sampling and an optimization method. *IEEE Transactions on Intelligent Transportation Systems*, 19(2):613–626, 2018.

[2] Claudiu Pozna, Fritz Troester, Radu Emil Precup, József K. Tar, and Stefan Preitl. On the design of an obstacle avoiding trajectory: Method and simulation. *Mathematics and Computers in Simulation*, 79(7):2211–2226, 2009.

[3] Xuemin Hu, Long Chen, Bo Tang, Dongpu Cao, and Haibo He. Dynamic path planning for autonomous driving on various roads with avoidance of static and moving obstacles. *Mechanical Systems and Signal Processing*, 100:482–500, 2018.

[4] Chongfeng Wei, Richard Romano, Natasha Merat, Y. Wang, C. Hu, H. Taghavifar, Foroogh Hajiseyedjavadi, and Erwin R. Boer. Risk-based autonomous vehicle motion control with considering human driver's behaviour. *Transportation Research Part C: Emerging Technologies*, 107(September 2018):1–14, 2019.

[5] R Craig Coulter. Implementation of the pure pursuit path tracking algorithm. Technical report, Carnegie-Mellon UNIV Pittsburgh PA Robotics INST, 1992.

[6] Chih-Lyang Hwang, Chang-Chia Yang, and John Y Hung. Path tracking of an autonomous ground vehicle with different payloads by hierarchical improved fuzzy dynamic sliding-mode control. *IEEE Transactions on Fuzzy Systems*, 26(2):899–914, 2017.

[7] Kibeom Lee, Seungmin Jeon, Heegwon Kim, and Dongsuk Kum. Optimal path tracking control of autonomous vehicle: Adaptive full-state linear quadratic gaussian (lqg) control. *IEEE Access*, 7:109120–109133, 2019.

[8] Plamen Petrov and Fawzi Nashashibi. Modeling and nonlinear adaptive control for autonomous vehicle overtaking. *IEEE Transactions on Intelligent Transportation Systems*, 15(4):1643–1656, 2014.

[9] Brian Paden, Michal Čáp, Sze Zheng Yong, Dmitry Yershov, and Emilio Frazzoli. A survey of motion planning and control techniques for self-driving urban vehicles. *IEEE Transactions on Intelligent Vehicles*, 1(1):33–55, 2016.

[10] Matthew Brown, Joseph Funke, Stephen Erlien, and J. Christian Gerdes. Safe driving envelopes for path tracking in autonomous vehicles. *Control Engineering Practice*, 61:307–316, 2017.

[11] Jiechao Liu, Paramsothy Jayakumar, Jeffrey L. Stein, and Tulga Ersal. A nonlinear model predictive control formulation for obstacle avoidance in high-speed autonomous ground vehicles in unstructured environments. *Vehicle System Dynamics*, 56(6):853–882, 2018.

[12] John Wurts, Jeffrey L. Stein, and Tulga Ersal. Collision Imminent Steering at High Speeds on Curved Roads Using One-Level Nonlinear Model Predictive Control. *IEEE Access*, 9(8):39292–39302, 2021.

[13] Eugenio Alcalá, Vicenç Puig, and Joseba Quevedo. LPV-MPC Control for Autonomous Vehicles. *IFAC-PapersOnLine*, 52(28):106–113, 2019.

[14] Huarong Zheng, Rudy R. Negenborn, and Gabriel Lodewijks. *Trajectory tracking of autonomous vessels using model predictive control*, volume 19. IFAC, 2014.

[15] Efstathios Siampis, Efstathios Velenis, and Stefano Longo. Rear wheel torque vectoring model predictive control with velocity regulation for electric vehicles. *Vehicle System Dynamics*, 53(11):1555–1579, 2015.

[16] Guilherme V Raffo, Guilherme K Gomes, Julio E Normey-Rico, Christian R Kelber, and Leandro B Becker. A predictive controller for autonomous vehicle path tracking. *IEEE transactions on intelligent transportation systems*, 10(1):92–102, 2009.

[17] Shuo Cheng, Liang Li, Ming-ming Mei, Yu-liang Nie, and Lin Zhao. Multiple-objective adaptive cruise control system integrated with dyc. *IEEE Transactions on Vehicular Technology*, 68(5):4550–4559, 2019.

[18] Jie Ji, Amir Khajepour, Wael William Melek, and Yanjun Huang. Path planning and tracking for vehicle collision avoidance based on model predictive control with multiconstraints. *IEEE Transactions on Vehicular Technology*, 66(2):952–964, 2017.

[19] Kyoungseok Han, Giseo Park, Gokul S Sankar, Kanghyun Nam, and Seibum B Choi. Model predictive control framework for improving vehicle cornering performance using handling characteristics. *IEEE Transactions on Intelligent Transportation Systems*, 22(5):3014–3024, 2020.

[20] Qingjia Cui, Rongjun Ding, Chongfeng Wei, and Bing Zhou. Path-tracking and lateral stabilisation for autonomous vehicles by using the steering angle envelope. *Vehicle System Dynamics*, 59(11):1672–1696, 2021.

[21] Hongbin Ren, Sizhong Chen, Lin Yang, and Yuzhuang Zhao. Optimal path planning and speed control integration strategy for ugvs in static and dynamic environments. *IEEE Transactions on Vehicular Technology*, 69(10):10619–10629, 2020.

[22] Yiqi Gao, Andrew Gray, H Eric Tseng, and Francesco Borrelli. A tube-based robust nonlinear predictive control approach to semiautonomous ground vehicles. *Vehicle System Dynamics*, 52(6):802–823, 2014.

[23] Jiaxing Yu, Xuexun Guo, Xiaofei Pei, Zhenfu Chen, Maolin Zhu, and Bian Gong. Robust model predictive control for path tracking of autonomous vehicle. Technical report, SAE Technical Paper, 2019.

[24] Jongsang Suh, Heungseok Chae, and Kyongsu Yi. Stochastic model-predictive control for lane change decision of automated driving vehicles. *IEEE Transactions on Vehicular Technology*, 67(6):4771–4782, 2018.

[25] A Wischnewski, M Euler, S Gümüs, and B Lohmann. Tube model predictive control for an autonomous race car. *Vehicle System Dynamics*, 60(9):3151–3173, 2022.

[26] Peng Hang, Xin Xia, Guang Chen, and Xinbo Chen. Active safety control of automated electric vehicles at driving limits: A tube-based mpc approach. *IEEE Transactions on Transportation Electrification*, 8(1):1338–1349, 2021.

[27] Liang Li, Yishi Lu, Rongrong Wang, and Jie Chen. A three-dimensional dynamics control framework of vehicle lateral stability and rollover prevention via active braking with mpc. *IEEE Transactions on Industrial Electronics*, 64(4):3389–3401, 2016.

[28] David Q Mayne, María M Seron, and SV Raković. Robust model predictive control of constrained linear systems with bounded disturbances. *Automatica*, 41(2):219–224, 2005.

[29] Pornchai Bumroongsri and Soorathep Kheawhom. Robust model predictive control with time-varying tubes. *International Journal of Control, Automation and Systems*, 15(4):1479–1484, 2017.

[30] Pornchai Bumroongsri. Tube-based robust mpc for linear time-varying systems with bounded disturbances. *International Journal of Control, Automation and Systems*, 13(3):620–625, 2015.

[31] Gonçalo Collares Pereira, Pedro F Lima, Bo Wahlberg, Henrik Pettersson, and Jonas Mårtensson. Linear time-varying robust model predictive control for discrete-time nonlinear systems. In *2018 IEEE Conference on Decision and Control (CDC)*, pages 2659–2666. IEEE, 2018.

[32] Toru Fujinaka and Mituhiko Araki. Discrete-time optimal control of systems with unilateral time-delays. *Automatica*, 23(6):763–765, 1987.

[33] Shaobing Xu, Huei Peng, and Yifan Tang. Preview path tracking control with delay compensation for autonomous vehicles. *IEEE Transactions on Intelligent Transportation Systems*, 22(5):2979–2989, 2020.

[34] Eunjae Lee, Hojin Jung, and Seibum Choi. Tire lateral force estimation using kalman filter. *International Journal of Automotive Technology*, 19(4):669–676, Aug 2018.

[35] M. Doumiati, A. C. Victorino, A. Charara, and D. Lechner. Onboard real-time estimation of vehicle lateral tire–road forces and sideslip angle. *IEEE/ASME Transactions on Mechatronics*, 16(4):601–614, 2011.

[36] Jacob Svendenius and Magnus Gäfvert. A brush-model based semi-empirical tire-model for combined slips. *SAE Technical Papers*, 2004(724), 2004.

[37] Hans Pacejka. *Tire and vehicle dynamics*. Elsevier, 2005.

[38] Chuan Hu, Rongrong Wang, Fengjun Yan, and Nan Chen. Should the desired heading in path following of autonomous vehicles be the tangent direction of the desired path? *IEEE Transactions on Intelligent Transportation Systems*, 16(6):3084–3094, 2015.

[39] Arthur Richards. Robust model predictive control for time-varying systems. In *Proceedings of the 44th IEEE Conference on Decision and Control*, pages 3747–3752. IEEE, 2005.

[40] Clemens Satzger, Ricardo de Castro, and Andreas Knoblach. Robust linear parameter varying model predictive control and its application to wheel slip control. *IFAC-PapersOnLine*, 50(1):1514–1520, 2017.

[41] Morris Kline. *Calculus: an intuitive and physical approach*. Courier Corporation, 1998.

[42] David Q Mayne, James B Rawlings, Christopher V Rao, and Pierre OM Scokaert. Constrained model predictive control: Stability and optimality. *Automatica*, 36(6):789–814, 2000.

[43] James Blake Rawlings, David Q Mayne, and Moritz Diehl. *Model predictive control: theory, computation, and design*, volume 2. Nob Hill Publishing Madison, WI, 2017.

Jonghyup Lee received the B.S., M.S and Ph.D degrees in mechanical engineering from Korea Advanced Institute of Science and Technology (KAIST), Deajeon, Korea, in 2015, 2017 and 2023, respectively. He has since taken the position of Senior Research Engineer at Hyundai Motor Company in 2023. His current research interests include vehicle dynamics and control, control theory, and autonomous driving systems.

Yoonjin Hwang received the B.S. degree in physics and mechanical engineering from Sogang University, Seoul, South Korea, in 2013 and the M.S. degree in mechanical engineering from Korea Advanced Institute of Science and Technology(KAIST), Daejeon, South Korea in 2015, where he is currently working toward the Ph.D. degree. His research interests include sensor fusion for localization and state estimation, vehicle dynamics, and autonomous vehicles.

Seibum.B.Choi received B.S. degree in mechanical engineering from Seoul National University, Korea, M.S. degree in mechanical engineering from Korea Advanced Institute of Science and Technology (KAIST), Korea, and the Ph.D. degree in controls from the University of California, Berkeley in 1993. Since 2006, he has been with the faculty of the Mechanical Engineering department at KAIST. His research interests include fuel saving technology, vehicle dynamics and control, and application of self-energizing mechanism.